# Toward Intelligent Design and Measurement of MEMS Acoustic Wave Resonators

Xingyu Liu, Tianxi Meng, Shuhan Chen, *Graduate Student Member, IEEE*, Tae Hoon Yang, Jun Zhang, *Fellow, IEEE*, Songbin Gong, and Yansong Yang, *Senior Member, IEEE* 

Abstract—Surface acoustic wave (SAW) resonators are a cornerstone in 5G/6G radio-frequency (RF) front ends owing to their compact form factor, strong electromechanical coupling, and compatibility with massive wafer-level manufacturability. Despite these advantages, conventional design-test workflows remain heavily reliant on full-wave multiphysics simulations, repeated tape-outs, and exhaustive vector network analyzer (VNA) sweeps. Such processes incur high cost, long iteration cycles, and limited scalability, while spurious modes and parasitic effects are difficult to capture accurately. To overcome these challenges, an AI-driven design-test prediction framework is developed to accelerate modeling, validation, and optimization of SAW resonators. A comprehensive dataset comprising 14,883 industry-verified devices, 10,000 simulated structures, and 283 fabricated samples is utilized for training and evaluation. The framework predicts basic metrics with coefficient determination  $(R^2) > 0.99$ . It further reconstructs admittance spectra directly from structural parameter inputs using ensemble regressors, yielding mean-squared error (MSE) on the order of 10<sup>-3</sup> and enabling accurate identification of spurious responses. Furthermore, a CNN-based sparse recovery method reconstructs spectra with only 16 frequency points, representing a 98% reduction from the original 1,024 points, while preserving  $R^2 > 0.98$ . Beyond prediction, an AIassisted process design kit (PDK) supports generative design: given target constraints, the system automatically synthesizes previously unseen, spurious-free resonators whose predicted spectra align with measurements, expanding the PDK with validated designs. Together, these capabilities bridge design and fabrication, substantially reduce simulation and measurement burden, and provide a scalable path toward AIdriven design automation of MEMS acoustic devices for nextgeneration RF applications.

Index Terms—Surface acoustic wave (SAW) resonators; MEMS; artificial intelligence (AI); Convolutional Neural Network (CNN); spectrum reconstruction; spurious mode analysis; sparse recovery; process design kit (PDK).

Manuscript submitted September 05, 2025; This work was supported in part by the National Natural Science Foundation of China under Grant 62304193, in part by the Hong Kong Innovation and Technology Commission under Grant ITS/144/23, and in part by the Hong Kong RGC Strategic Topic Grant under Grant STG3/E-602/23N. (Corresponding author: Yansong Yang).

Xingyu Liu, Tianxi Meng, Shuhan Chen, Jun Zhang, and Yansong Yang are with the Department of Electronic and Computer Engineering, the Hong Kong University of Science and Technology, Hong Kong (e-mail: xliufs@connect.ust.hk; <a href="mailto:eeyyang@ust.hk">eeyyang@ust.hk</a>).

Songbin Gong is with Spectron Technology Co., Ltd, Shenzhen, China. Tae Hoon Yang is with Stanford University, CA, USA.

Color versions of one or more of the figures in this article are available online at <a href="http://ieeexplore.ieee.org">http://ieeexplore.ieee.org</a>.

Digital Object Identifier

#### I. INTRODUCTION

HE rapid evolution of wireless communication standards toward 5G and 6G has placed unprecedented on radio-frequency demands (RF) components. Surface acoustic wave (SAW) devices remain indispensable in this context due to their compact form factor, inherently low insertion loss, and compatibility with largescale manufacturing [1]. To support higher frequency bands, wider bandwidths, and stricter linearity requirements, significant efforts have been made to engineer both substrate materials [2], [3], [4], [5] and device architectures [6], [7], [8] are being explored. Among these advances, the 42° Y-cut, Xpropagating lithium tantalate (42° YX LT) substrate has gained prominence as a cornerstone technology. It provides a favorable balance of electromechanical coupling, temperature stability, and achievable quality factor (Q), positioning it as a leading candidate for next-generation RF filters [9], [10]. Recent developments such as piezoelectric-on-insulator (POI) and incredible high-performance (IHP) SAW structures [11], [12] have further extended the utility of 42° YX LT, enabling improved energy confinement, enhanced O values, and wider design flexibility.

Despite these advantages, the design and optimization of such MEMS-based acoustic resonators, particularly for waferlevel fabrication processes, still face several practical bottlenecks. Like other vibrating MEMS devices, targeted SAW resonators are also highly sensitive to process variations across foundries, leading to deviations in key performance metrics such as spurious modes, electromechanical coupling  $(k_t^2)$ , and O [13], [14]. The conventional development cycle remains heavily reliant on iterative full-wave electromagnetic (EM)-acoustic simulations, followed by multiple tape-outs and measurement steps for model verification and tuning. This workflow is inherently time-consuming and labor-intensive [15], [16], particularly when extended to wafer-level yield prediction or large-scale design space exploration. Furthermore, spurious responses [17] and subtle parasitic effects [18], [19] are often difficult to capture accurately in physics-based compact models, adding to the reliance on empirical correction after fabrication. These constraints slow down innovation and limit the scalability of acoustic resonator design for mass production, at a time when the market is rapidly expanding with application-specific requirements for

Comparison	Yan et al. [20]	Liu et al. [21]	Akinwande et al. [22]	Sui et al. [23]	Zhang et al. [24]	Zuo et al. [25]	This Work
Multi-targeted objective	No	Yes	Yes	No	Yes	Yes	Yes
Optimization methodology	Single target	Multi targets	Multi targets	Multi targets	Multi targets	Multi targets	Multi targets
<b>Database utilization</b>	No	Yes	Yes	Yes	Yes	Yes	Yes
Automatic design	No	Yes	Yes	Yes	Yes	Yes	Yes
Simulations independence	No	No	Low	High	High	High	High
Measurement efficiency	No	No	No	No	Partial	No	Yes
Scalability	Costly	No	No	No	No	No	Yes
Experimental validation	Yes	No	No	Yes	Yes	Yes	Yes

TABLE I
STATE OF THE ART OF THE AI-BASED MICROELECTRONICS AND MICROSYSTEMS

diverse 5G/6G bands [26].

Recent advances in artificial intelligence (AI) offer a compelling opportunity to address the long-standing limitations in microelectronics and microsystems design. AI techniques have already demonstrated substantial impact in electronic design automation (EDA) [27], circuit modeling [28], and process variation prediction [29]. Table I provides a state-of-the-art comparison of representative approaches, including spanning traditional fabrication-driven methods [20], machine-learning-assisted design frameworks shown in [21], [23], transfer learning for EM modeling [22], device-level optimization in acoustic resonators [24], and multi-target inverse design algorithms [25]. As highlighted in Table I, earlier works are often limited to single-target optimization or rely heavily on large-scale simulations, with scalability and experimental validation remaining significant challenges. In contrast, the proposed work achieves a multi-targeted objective, covering both performance metrics and fullspectrum reconstruction, while demonstrating simulationefficient modeling, sparse measurement recovery, and waferlevel scalability with experimental validation. This positions this work as a unified AI-driven pipeline that bridges design automation, simulation reduction, fabrication-oriented, and large-scale measurement validation.

In this study, an AI-driven design—test framework for SAW resonators is investigated. Specifically, physics-informed regressors are developed to predict key scalar metrics and to reconstruct the full admittance spectrum; a CNN-based sparse-spectrum recovery enables fast wafer-level testing; spurious-

mode quantification guides suppression strategies; and an AI-assisted PDK supports both forward prediction and generative inverse design of new, spurious-free structures. Section II details the modeling pipeline and the multi-physics equations used for interpretability. Section III reports modeling and measurement results on a mixed dataset. Lastly, a brief conclusion is provided in Section IV.

#### II. ACOUSTIC RESONATOR DESIGN METHODOLOGY

The traditional process flows for MEMS acoustic resonator production, especially mass production, require these devices to be manually designed, iteratively simulated, and fabricated round by round, with final fine frequency-domain measurements. While this approach ensures accuracy, it inevitably incurs heavy reliance on full-wave simulations and multiple tape-outs, leading to time-consuming iterations, high costs, and limited scalability at the wafer level. Such bottlenecks restrict rapid exploration of the design space and hinder efficient performance optimization.

Recent progress in artificial intelligence provides an alternative path that AI models can serve as accelerators within the resonator design loop shown in Fig. 1. Integrating a modeling engine into the feedback cycle allows structural parameters and sparse sampling data to be directly mapped to key device metrics and even the full admittance spectrum. This enables prediction without exhaustive simulations, recovery of dense responses from limited measurements, and compensation across wafers. In this way, the loop evolves from a resource-intensive cycle into an AI-augmented

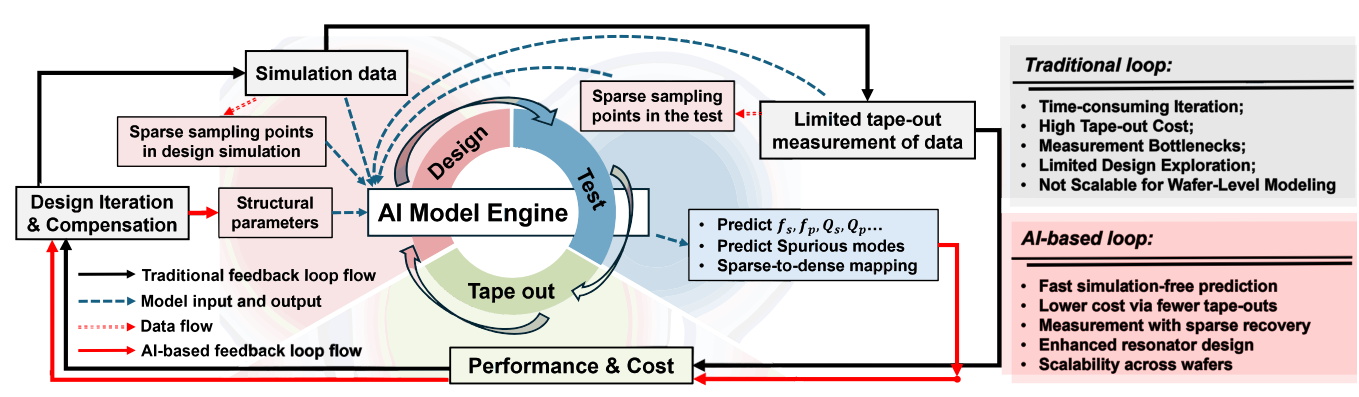


Fig. 1. AI-accelerated design-test-tape out loop for performance and cost optimization.

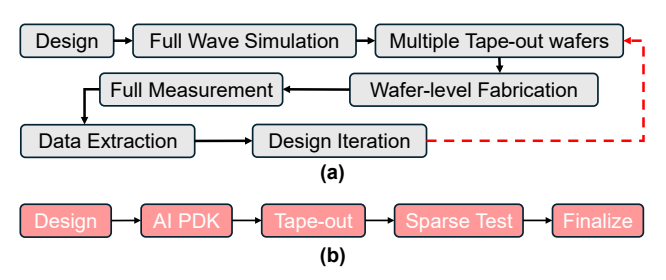


Fig. 2. Comparison of (a) traditional and (b) AI-driven design-test flows for SAW resonators.

framework capable of fast, low-cost, and scalable optimization. To simplify, Fig. 2 compares the conventional design-test loop with the AI-driven alternative. In the traditional workflow [Fig. 2(a)], repeated simulations, tape-outs, and full measurements are required, resulting in high cost and limited scalability. By contrast, the AI-assisted workflow [Fig. 2(b)] relies on a parametric design library and sparse testing to achieve faster validation and more efficient wafer-level optimization.

# A. Normal SAW Resonators' Design-Test Framework

Traditionally, the design-test workflow is initiated by specifying a target operating frequency for the intended devices, such as the desired filters [30], oscillators [31], duplexers [32], wireless tags or sensors [33], which relies on the relation between elastic wave propagation in solids and the geometrical periodicity of the interdigital transducer (IDT) structure. For a deformable solid, the local form of Newton's second law reads:

$$\rho \frac{dv_i}{dt} = \rho F_i + \frac{\partial \sigma_{ij}}{\partial x_j} \tag{1}$$

where  $\rho$  is the density,  $v_i$  the particle velocity, and  $\sigma_{ij}$  the stress tensor. Assuming small deformations, the linear stress–strain relation generalizes Hooke's law:

$$\sigma_{ij} = c_{ijkl} \, \varepsilon_{kl}, \tag{2}$$

$$\varepsilon_{kl} = \frac{1}{2} \left( \frac{\partial u_k}{\partial x_l} + \frac{\partial u_l}{\partial x_k} \right) \tag{3}$$

where u is the displacement vector and  $c_{ijkl}$  the stiffness tensor. For an isotropic medium, Eq. (1) reduces to the wave equation:

$$\rho \frac{\partial^2 \mathbf{u}}{\partial t^2} = (\lambda + 2\mu) \nabla (\nabla \cdot \mathbf{u}) - \mu \nabla \times (\nabla \times \mathbf{u})$$
 (4)

where  $\lambda$  and  $\mu$  are the Lamé constants. This admits two bulk wave solutions with distinct velocities:

$$V_L = \sqrt{\frac{\lambda + 2\mu}{\rho}}, \qquad V_T = \sqrt{\frac{\mu}{\rho}}$$
 (5)

Considering a plane sinusoidal wave of the form  $\mathbf{u}(x,t) =$ 

 $u_0 e^{j(\omega t - kx)}$ , the dispersion relation is obtained:

$$k = \frac{2\pi}{\lambda}, \quad \omega = 2\pi f, \quad v_{\rm ph} = \frac{\omega}{k}$$
 (6)

In the case of Rayleigh waves propagating on the free surface of a semi-infinite isotropic solid, the velocity  $V_R$  is given by the secular equation involving  $V_L$  and  $V_T$  [34]:

$$\left(2 - \frac{V_R^2}{V_T^2}\right)^2 = 4\sqrt{\left(1 - \frac{V_R^2}{V_T^2}\right)\left(1 - \frac{V_R^2}{V_L^2}\right)} \tag{7}$$

Since  $V_R$  depends only on the material properties  $(\lambda, \mu, \rho)$  and not on frequency, the operating frequency of a SAW device is explicitly determined by the IDT pitch:

$$f_0 = \frac{V_R}{\lambda} = \frac{V_R}{2 \times Pitch} \tag{8}$$

where  $\lambda$  corresponds to the acoustic wavelength set by the electrode periodicity, and Pitch is the sum of electrode width and gap. For 42° YX LT,  $V_R$  should reach around 4211 m/s [14]. Then, the coupling coefficient is tuned via electrode duty cycle and normalized thickness  $h_{sub}/\lambda$  [3], where  $h_{sub}$  means the thickness of substrate, which is labeled in Fig. 3. The electromechanical coupling coefficient ( $k_t^2$ ) quantifies how efficiently electrical energy is converted into acoustic wave energy in piezoelectric media and SAW devices. For a linear piezoelectric solid under small strains, the coupled equations are:

$$T = c^{E}S - e^{TE}.D = eS + \varepsilon^{S}E$$
 (9)

where T, S are stress and strain, E, D are electric field and displacement,  $c^E$  is the elastic stiffness at constant field,  $\varepsilon^S$  is the permittivity at constant strain, and e is the piezoelectric matrix. The time-averaged energy density of a harmonic wave is:

$$W = \frac{1}{2} (\mathbf{S}^T \mathbf{T} + \mathbf{E}^T \mathbf{D}) \tag{10}$$

For a given vibration mode M, the dimensionless coupling coefficient  $K_M^2$  measures the fraction of total energy that can be exchanged between electrical and mechanical domains. A convenient form compares the phase velocities under openand short-circuited electrical boundary conditions:

$$K_M^2 = \frac{v_{\text{open}}^2 - v_{\text{short}}^2}{v_{\text{open}}^2} \approx 2 \frac{v_{\text{open}} - v_{\text{short}}}{v_{\text{open}}}$$
(11)

This expression highlights that the velocity reduction induced by short-circuit boundary conditions is a direct measure of electromechanical coupling strength. In one-dimensional approximations (thickness or oriented single axis), Eq. (11) reduces to the commonly cited material form:

$$K^2 \approx \frac{e_{ij}^2}{\varepsilon_{ii} \, c_{jj}^E} \tag{12}$$

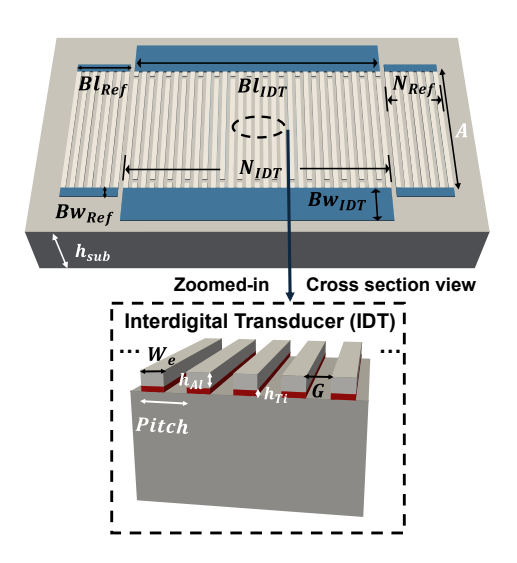


Fig. 3. Illustration of SAW resonator and zoomed in IDT layout.

with  $e_{ij}$ ,  $\varepsilon_{ii}$ ,  $c_{jj}^E$  being the relevant material constants. This provides a material-level indicator of the intrinsic coupling strength. In practical SAW resonators, electrode mass loading, electrical loading, and acoustic radiation modify the observable resonance behavior. The effective coupling coefficient  $k_t^2$  is therefore defined from the measurable resonance  $(f_s)$  and anti-resonance  $(f_p)$  frequencies [35]:

$$k_t^2 = \left(\frac{\pi}{2} \times \frac{f_s}{f_p}\right) / \tan\left(\frac{\pi}{2} \times \frac{f_s}{f_p}\right)$$
(13)

For practical calculations, the  $k_t^2$  can be approximated as:

$$k_t^2 \approx \frac{\pi^2}{8} \cdot \frac{f_p^2 - f_s^2}{f_s^2}$$
 (14)

Consider a one-port resonator characterized by input admittance  $Y_{11}(f) = G(f) + jB(f)$  (or reflection  $S_{11}(f)$ ) referenced to  $Z_0 = 50 \Omega$ . The quality factor of a resonator is defined as the ratio between the resonance frequency and the corresponding 3-dB bandwidth. At the series resonance  $f_s$ , this yields the series quality factor  $Q_s = f_s/\Delta$ , while at the parallel

TABLE II STRUCTURAL PARAMETERS IN SAW DEVICE DESIGN

Symbol	Description	Training
A [μm]	Aperture	Included
$N_{IDT}$	Number of IDT electrodes	Included
$N_{Ref}$	Number of reflector fingers	Excluded
$W_e$ [um]	Electrode width	Included
G [um]	Electrode gap	Included
Pitch [µm]	Electrode pitch: $W_e + G$	Included
MR	Metal ratio: We / Pitch	Included
$h_{Al}$ [nm]	Al thickness	Included
$h_{Ti}$ [nm]	Ti thickness	Included
$h_{sub}$ [µm]	Substrate thickness	Included
$Bw_{IDT}$ [um]	Busline width of IDT	Excluded
$Bw_{Ref}$ [um]	Busline width of reflector	Excluded
$Bw_{IDT}$ [um]	Busline length of IDT	Excluded
$Bw_{Ref}$ [um]	Busline length of reflector	Excluded

resonance  $f_p$ , the parallel quality factor is similarly given by  $Q_p = f_p/\Delta f_p$ . Both quantities characterize the energy storage relative to loss at the respective resonance and anti-resonance frequencies.

For a loss-limited single-port described by reflection coefficient  $\Gamma(f) = S_{11}(f)$ , the Bode Q is defined from the frequency-sensitivity of the input impedance (equivalently, the phase slope of  $\Gamma$ ):

$$Q_{\text{Bode}}(f) = \frac{\omega \, \tau_g(f) \, |\Gamma(f)|}{1 - |\Gamma(f)|^2}, \omega = 2\pi f, \, \tau_g(f) \triangleq -\frac{\partial \arg \Gamma}{\partial \omega} \quad (15)$$

Using numerical differentiation with frequency in Hz, this can be evaluated as

$$Q_{Bode}(f) = \frac{2\pi f \left[ -\frac{\partial \arg S_{11}}{\partial f} \right] |S_{11}(f)|}{1 - |S_{11}(f)|^2}$$
(16)

This expression is exactly what we compute in code to obtain a frequency-dependent  $Q_{\text{Bode}}(f)$ ; the reported  $Q_{max}$  is the maximum within  $[f_s, f_p]$ .

The design of SAW resonators, fundamentally, considering all the performance metrics mentioned above, begins with the determination of key structural parameters, such as the

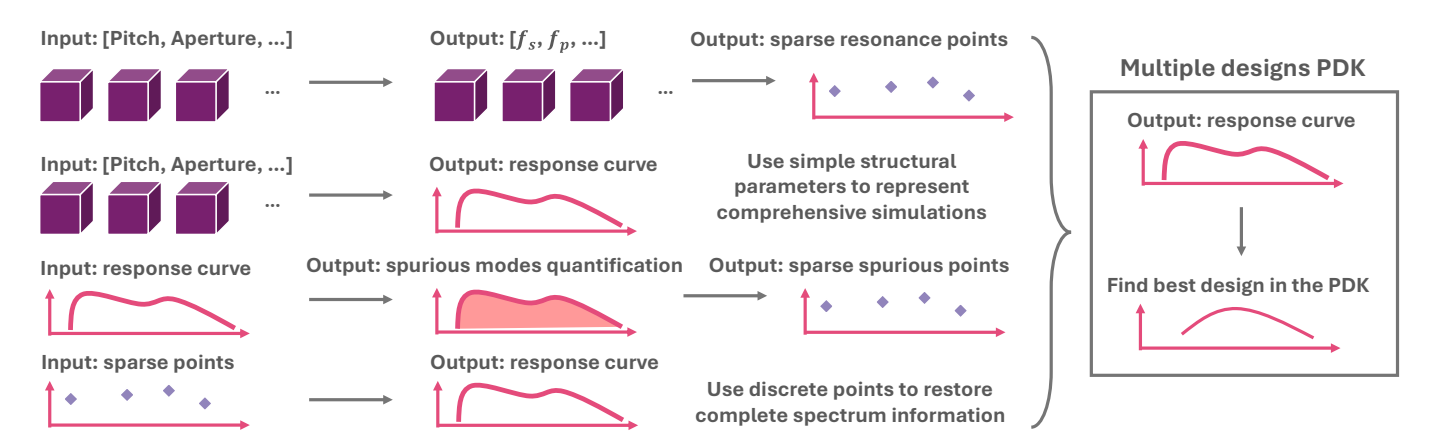


Fig. 4. AI-based design-test pipeline for SAW resonators.

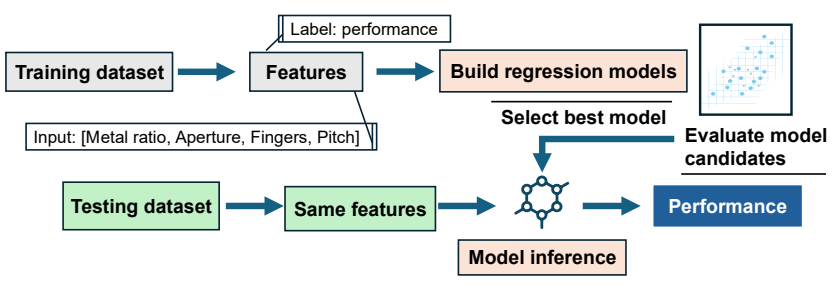


Fig. 5. Workflow of performance metric prediction using regression models.

electrode pitch and the LiTaO<sub>3</sub> substrate thickness. Once these are specified, the conventional workflow relies on iteratively tuning a broad set of structural variables, as illustrated in Fig. 3 and summarized in Table II, using multiphysics simulations to achieve the desired performance.

However, these parameter variations not only affect the acoustic properties of the target resonance mode but also introduce undesired spurious responses, originating from other acoustic modes or even EM coupling. This makes the optimization process highly dependent on fine parameter adjustments and repeated simulations, creating substantial design overhead. Even if an apparently optimal configuration is identified through simulation, process-induced variations during fabrication pose another critical challenge. Systematic deviations in dimensions or film thickness, unavoidable in fixed manufacturing processes, can shift the device away from its intended operating point. As a result, the fabricated resonator may fail to deliver the simulated optimum, forcing repeated cycles of redesign and re-optimization in order to meet performance specifications. Meanwhile, at the wafer level, production testing introduces further inefficiencies. Accurate characterization requires wideband frequency sweeps with fine resolution to capture resonance and spurious behavior. Since each frequency point measured by the vector network analyzer (VNA) incurs non-negligible computation time, scaling this procedure to hundreds or thousands of devices on a single wafer results in prohibitive measurement cost and time.

#### B. Multi-Stage AI Modeling Pipeline

The proposed AI-based framework replaces simulation-

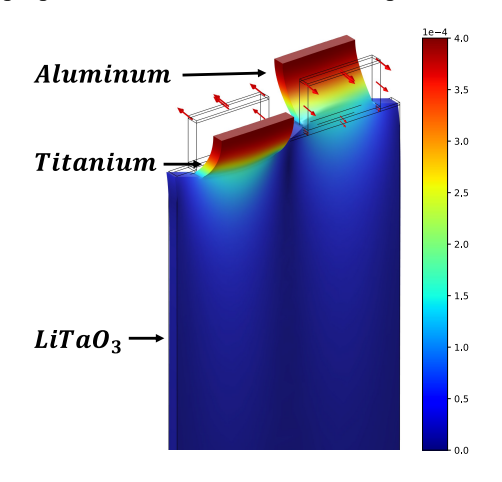


Fig. 6. COMSOL simulation model of Al/Ti on a LiTaO3 substrate.

TABLE III
PREDICTIVE ACCURACY OF BASELINE MODELS

Model	MSE	$R^2$
Ridge	0.0102	0.9899
Lasso	0.2896	0.6304
Elastic Net	0.0823	0.9195
Gradient Boosting	0.0049	0.9951
Random Forest	0.0034	0.9967
XGBoost	0.0028	0.9972
CatBoost	0.0031	0.9969

intensive and tape-out-dependent processes with a multi-stage modeling pipeline, as illustrated in Fig. 4. The pipeline begins with the prediction of scalar performance metrics, such as the resonance frequency ( $f_s$ ), anti-resonance frequency ( $f_p$ ), electromechanical coupling coefficient ( $k_t^2$ ), quality factors (including  $Q_s$ ,  $Q_p$ , and Bode Q), directly from basic structural parameters (e.g., A,  $N_{IDT}$ , Pitch, MR, and so on). This serves as an efficient substitute for multiphysics simulations when only a quick preliminary check is needed during early-stage design.

As illustrated in Fig. 5, the prediction of scalar performance metrics is formulated as a supervised regression task. A comprehensive training dataset is constructed from 10,000 simulated resonator responses generated through COMSOL parameter sweeps, aligned with the discussions in Section A, with the corresponding modeling settings shown in Fig.6. Each device structure is encoded into a feature vector, while the associated performance labels are extracted from simulation or measurement. Using this dataset, multiple regression models, including linear regressors, support vector regression, and ensemble tree methods, are trained and benchmarked on a held-out testing set.

Model performance is evaluated using two standard metrics: the mean squared error (MSE) [36]:

$$MSE = \frac{1}{n} \sum_{i=1}^{n} (y_i - \widehat{y_i})^2$$
 (17)

which quantifies the average squared difference between predicted values  $\hat{y}_i$  and ground truth values  $y_i$ , where n is the number of total samples.

Another is the coefficient of determination  $(R^2)$ :

$$R^{2} = 1 - \frac{\sum_{i=1}^{n} (y_{i} - \hat{y}_{i})^{2}}{\sum_{i=1}^{n} (y_{i} - \bar{y})^{2}}$$
(18)

where  $\bar{y}$  is the mean value of the ground truth values. A  $R^2$  score close to 1 indicates high predictive accuracy; a score less than 0 implies worse-than-mean performance.

As shown in Table III, ensemble tree-based methods such as Random Forests and XGBoost achieved the lowest prediction error and the highest  $R^2$  values. This superior accuracy can be attributed to their ability to capture complex nonlinear relationships and feature interactions among resonator structural parameters, which are not well modeled by linear baselines.

To extend beyond scalar performance metrics, the

framework incorporates full-spectrum reconstruction. An ExtraTrees regression model similar to the framework in Fig. 5 is employed to map structural parameters directly to the complete admittance response, including the real, imaginary, and magnitude components, which not only reproduces the main resonance but also resolves fine spectrum features, thereby enabling accurate virtual evaluation of device behavior without the need for exhaustive frequency-domain sweeps.

Given the critical role of parasitic resonances, spurious mode quantification is incorporated as an additional stage. In this step, vector fitting (VF) is applied to the admittance response to extract poles and identify secondary peaks that make significant contributions to spurious behavior. Based on these features, a spurious score (Sc) is defined by combining the number and strength of the extracted poles and peaks and is integrated as a complementary performance metric:

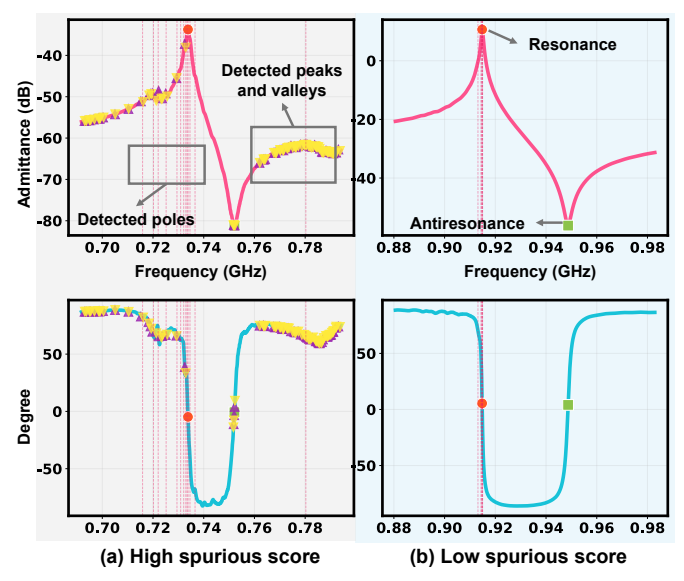


Fig. 7. Illustration of spurious score on resonator admittance Spectrum.

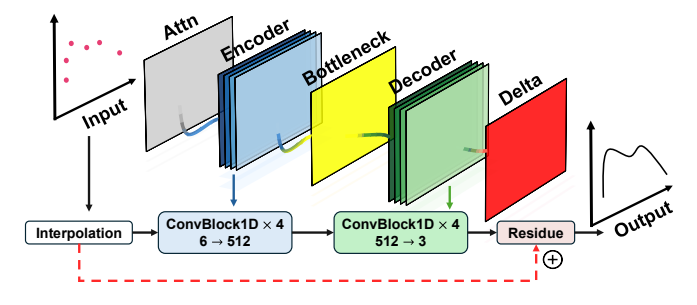


Fig. 8. Modified CNN framework for reconstructing full-resolution spectrum from sparse inputs.

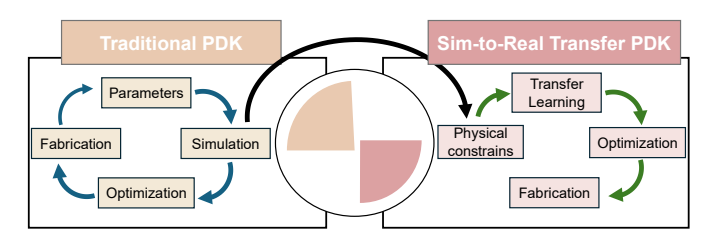


Fig. 9. Transition from simulation-only loop to sim-to-real transfer PDK

$$Sc = poles + peaks + valleys - 2$$
 (19)

Poles are extracted using the vector fitting (VF) algorithm, while peaks and valleys are identified by manual definition. This comparison, shown in Fig. 7, demonstrates that the spurious score can quantitatively distinguish resonators with different levels of spectral purity, enabling an objective assessment of spurious behavior. In this way, information on spurious responses, beyond the main resonances, can be systematically incorporated into subsequent modeling and optimization.

To further reduce modeling and data collection costs, the workflow transitions from full-band regression to a sparsespectrum recovery strategy. While tree-based regressors can predict fine-grained admittance curves, their model complexity and data requirements scale rapidly with increasing training size and spectrum resolution. To address this, a small set of informative discrete points, such as resonance and anti-resonance anchors, spurious peaks identified through vector fitting, and slope-change knots, is first extracted. A modified convolutional neural network (CNN) shown in Fig. 8 is then trained to reconstruct the complete admittance response from these sparse samples. The method is applicable both in simulation, by reducing the number of solver evaluations per structure, and in wafer-level testing, by shortening the number of VNA sweep points per device, thus delivering substantial efficiency gains without sacrificing spectral accuracy.

Finally, the outputs of all modeling stages are consolidated into an AI-assisted process design kit (PDK), just as shown in Fig. 9. The PDK stores multiple candidate designs, allows rapid comparison of performance curves, and supports layout-level optimization across frequency bands and fabrication conditions, enabling efficient reuse and fast iteration. Beyond serving as a design library, the PDK also embeds a simulation-to-real (Sim-to-Real) framework that leverages abundant simulated samples to reduce reliance on costly measurements, requiring only a small subset of experimental results for accurate calibration. This combined capability lowers the burden of wafer-level testing while enhancing the scalability of the AI-assisted workflow for practical resonator design.

# C. Detailed Models and Algorithms of Proposed Baseline

Just as mentioned in Section. B, the modeling pipeline begins by parsing filenames or design files to extract structural parameter vectors  $x \in R^d$  (e.g., A,  $N_{\rm IDT}$ , Pitch, MR, etc.), along with full admittance spectrum admittance  $Y(f) = [Y_{\rm Re}(f), Y_{\rm Im}(f), |Y(f)|_{\rm dB}] \in R^{3\times L}$  for either simulated or measured samples. These are aligned and persisted as  $\{X, Y, {\rm split}\}$ , where  $Y_{\rm Re}$  and  $Y_{\rm Im}$  denote the real and imaginary components, and  $|Y|_{\rm dB}$  represents the log-magnitude.

To predict scalar metrics, we train a family of regressors  $\mathcal{F} = \{\text{Ridge}, Random Forest, XGBoost, CatBoost ...}\}$  to map:

$$f_{\text{scalar}}: x \mapsto m = \left[ f_s, f_p, k_t^2, Q_s, Q_p, Q_{\text{Bode}} \right]$$
 (20)

Prediction accuracy is evaluated via mean squared error

(MSE) and coefficient of determination  $(R^2)$  shown in Eq. (17) and Eq. (18).

The full admittance spectrum is reconstructed by training two regressors:

$$g_{\rm R}, g_{\rm I}: x \mapsto \widehat{Y_{\rm Re}}, \widehat{Y_{\rm Im}} \in R^L,$$
 (21)

with the reconstructed log-magnitude computed as:

$$\left|\hat{Y}\right|_{dB} = 20 \log_{10} \left( \sqrt{\widehat{Y_{Re}^2 + \widehat{Y_{lm}^2}}} + \varepsilon \right)$$
 (22)

The total spectrum loss is defined as the following equation to have a faster convergence:

$$\mathcal{L}_{se} = 0.3 \text{ MSE}(Y_{Re}, \widehat{Y_{Re}}) + 0.3 \text{ MSE}(Y_{Im}, \widehat{Y_{Im}}) + 0.4 \text{ MSE}(|Y|_{dB}, |\widehat{Y}|_{dB})$$
(23)

Spurious behavior is quantified by first applying vector fitting to  $\hat{Y}(f)$  to extract poles  $\mathcal{P}$ , followed by detecting peak and valley indices  $\mathcal{K}_{pk}$  and  $\mathcal{K}_{vl}$  on the dB-magnitude curve. The spurious score is defined as:

$$S_c = |\mathcal{P}| + |\mathcal{K}_{pk}| + |\mathcal{K}_{vl}| - 2 \tag{24}$$

which aligns with Eq. (19).

A saliency-based subsampling strategy is applied by computing:

$$s(f_l) = w_1 |\nabla|Y||(f_l) + w_2 |\nabla^2|Y||(f_l)$$
 (25)

to allocate the sparse sampling set  $\mathcal{I} \subset \{1, ..., L\}$  with higher density near  $\widehat{f}_s$ ,  $\widehat{f}_p$  and local extrema.

Sparse reconstruction is performed using a masked U-Net with input tensor:

$$x = [Y_{\text{Re}}^{\mathcal{I}}, Y_{\text{Im}}^{\mathcal{I}}, |Y|_{\text{dB}}^{\mathcal{I}}, \text{ mask, freq-enc, } f_s / f_p \dots \text{-attn}]$$

$$x \in R^{6 \times L}$$
(26)

An interpolated prior  $\tilde{y}$  is generated and attention-modulated input is computed as:

$$x \leftarrow x \cdot (1 + \text{Conv1D}(x_{\text{attn}}))$$
 (27)

Deep CNNs such as AlexNet [37], VGG [38], and ResNet [39] established the foundations of modern image recognition, showing that deeper networks can be effectively trained and scaled [40]. However, these architectures mainly target global representation learning. For reconstruction tasks with sparse or incomplete inputs, U-Net [41] provides a more suitable encoder—decoder structure with skip connections, enabling both global context extraction and local detail preservation.

The network, which is based on the modified U-Net network, predicts the full spectrum  $\hat{Y} \in R^{3 \times L}$ , optimized under the composite loss, which is explained clearly by the following Algorithm 1.

After executing the entire modeling pipeline, including

```
Algorithm 1: Training of Masked U-Net for Spectrum Reconstruction
```

**Input:** Input tensor  $x \in \mathbb{R}^{6 \times L}$ , ground truth

```
y \in \mathbb{R}^{3 \times L}, epochs T, weight \alpha
   Output: Trained model f_{\theta}: \mathbb{R}^{6 \times L} \to \mathbb{R}^{3 \times L}
1 Initialize model parameters \theta;
2 for t=1 to T do
3
          foreach mini-batch (x, y) do
                 Interpolate: \widetilde{y} \leftarrow \text{Interp}(x_{\text{sparse}}, \text{mask});
4
                 Attention boost: x \leftarrow x \cdot (1 + \text{Conv1D}(x_{\text{attn}}));
5
                 Predict residual: \Delta y \leftarrow f_{\theta}(x);
                 Reconstruct: \hat{y} \leftarrow \widetilde{y} + \Delta y;
7
                Preserve sparse:
8
                   \hat{y} \leftarrow \hat{y} \cdot (1 - \text{mask}) + x_{\text{sparse}} \cdot \text{mask};
                Compute total loss:
9
                    \mathcal{L} = \alpha \mathcal{L}_{\text{reim}} + (1 - \alpha) \frac{1}{2} (\mathcal{L}_{\text{db}} + \mathcal{L}_{\text{pred}} + \mathcal{L}_{\text{cons}})
                   Backpropagate and update \theta
```

10 return  $f_{\theta}$ 

scalar metric prediction, full-spectrum reconstruction, spurious mode quantification, and sparse recovery, Overall, the complete output of each design is organized into the PDK entry:

$$x\mathcal{E} = \{x, f_{\text{scalar}}(x), \widehat{Y}(f), S_{c}\}$$
 (28)

enabling downstream selection and optimization, with optional Sim-to-Real calibration for measured alignment.

# III. RESULTS AND DISCUSSION

To validate the proposed AI-driven methodology, a set of  $42^{\circ}$  YX rotated lithium tantalate-based SAW resonators was simulated and fabricated. As summarized in Table II, the resonator performance is influenced by a complex interplay of structural parameters, among which a subset of 9 key variables in Table IV is selected as the models' input for training (Including  $W_e$  and G). The dataset consists of 14,883 deembedded admittance spectra from industry-verified structures, along with 10,000 simulated samples and 283 fabricated and measurement samples. The microscope image of fabricated devices is shown in Fig. 10. All samples have been screened to ensure physical validity and consistency

TABLE IV
SUBSET OF TUNABLE TYPICAL PARAMETERS FOR PRACTICAL AND
MODELING

Design Parameters	Simulation	Measurement	Verified data from industry*
A [μm]		36-272	36-216
$N_{IDT}$		31-241	31-241
Pitch [µm]	0.6-3.4	1.8-3.4	1.8-2.7
MR	0.35-0.7	0.4-0.7	0.4-0.65
$h_{Al}$ [nm]	70-450	220-450	350
$h_{Ti}$ [nm]	5-40	40	40
$h_{sub}$ [ $\mu$ m]	100-350	200	200

\* Accurate data verified by Spectron

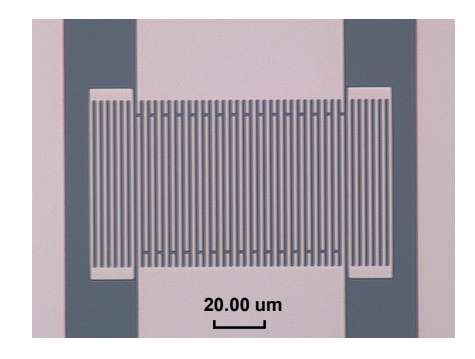


Fig. 10. Microscope image of one of fabricated devices.

across simulation domains.

# A. Performance Metrics Prediction Accuracy

To achieve the full design-test workflow, the first modeling stage aims to predict key performance parameters directly from the structural input vector, as illustrated in Fig. 11. Motivated by its superior fitting performance in simulations, the XGBoost model was applied to industrial-grade data, trained on 75% labeled 1D vectors of 14,883 industry-verified samples, as shown in Table III. As reported in Fig. 12, the

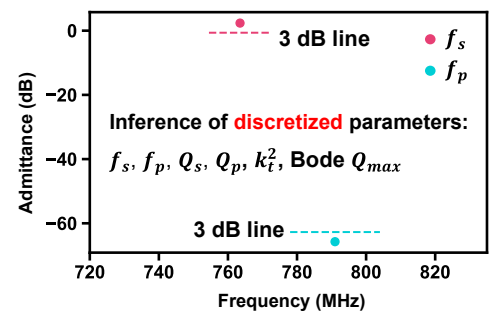


Fig. 11. Prediction of discretized resonator parameters from structural input.

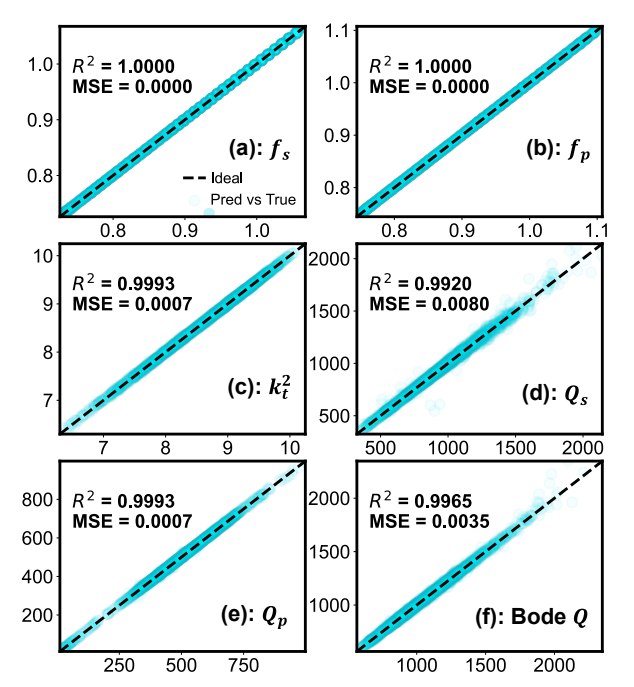


Fig. 12. Regression performance of XGBoost model on resonator parameters.

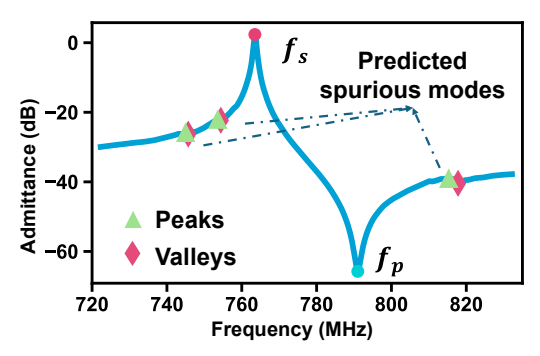


Fig. 13. Inference of admittance spectrum with clear identification of spurious responses.

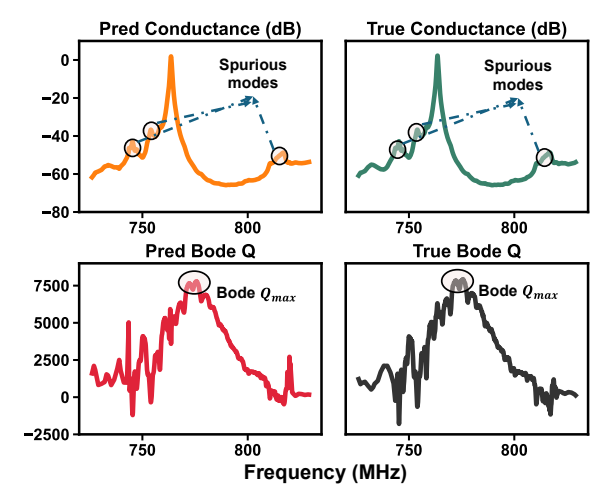


Fig. 14. Features matching in passband and spurious mode artifacts, while recovering the Bode Q profile with correct peak position and magnitude.

proposed regression model achieves nearly perfect agreement with the ground truth. Both the resonance and anti-resonance frequencies are predicted with  $R^2=1.0000$  and negligible mean squared error, demonstrating the capability to precisely capture frequency behavior. Similarly, the electromechanical coupling factor  $(k_t^2)$  and quality factors  $(Q_s, Q_p)$  are reproduced with  $R^2>0.99$ , while the Bode quality factor maintains high accuracy with  $R^2=0.9965$ . These results confirm that the regression model can reliably extract both frequency and quality metrics from structural parameters.

# B. Admittance Reconstruction with Accurate Spurious Modes

To enable spurious mode analysis and band-edge evaluation shown in Fig. 13, the full admittance spectrum is predicted from structural inputs like Section A using the ExtraTrees model, whose fitting ability on the related dataset is further enhanced through hyperparameter optimization with Optuna. Representative results shown in Fig. 14 illustrate close alignment between predicted and verified responses across main and spurious modes, while correctly reproducing the Bode Q profile and its maximum. Key performance parameters extracted from the predicted spectrum are summarized in Table V. Across the 25% held-out test set, the coefficient of determination of admittance prediction remained above 0.99 with mean squared errors in the order of  $10^{-3}$ , confirming that the proposed approach reliably supports

frequency-domain design verification. Compared with full-wave simulations and repeated measurements, this predictive framework substantially reduces computational and experimental cost while preserving accuracy in spurious mode identification.

TABLE V

COMPARISON OF GROUND TRUTH AND RESONATOR PARAMETERS
EXTRACTED FROM PREDICTED ADMITTANCE

Parameters	True	Pred	Error
$f_s$ (GHz)	0.763	0.764	0.0013
$f_p$ (GHz)	0.791	0.791	0.0000
$k_t^2$ (%)	9.05	8.98	0.0077
$Q_s$	146.0	146.7	0.0048
$Q_p$	158.2	158.2	0.0000
Bode $Q_{max}$	7932.3	7787.4	0.0183
Bode Q Freq. (GHz)	0.776	0.775	0.0013

# C. Sparse Spectrum Recovery Using CNN

After identifying the resonance points and spurious mode locations, a down-sampling process is applied to reduce the full 26,000-point admittance spectrum to 1,024 representative frequency points, as illustrated in Fig. 15. In this framework, only a small set of informative anchor points is retained, such as resonance and anti-resonance frequencies, spurious peaks identified by vector fitting, and slope-change features, which serve as the minimal descriptors of each device response. Around these critical points, dense sampling is applied to accurately capture local spectral variations, while the remaining regions are sampled more coarsely to reduce overall data requirements.

To further reduce both modeling and data-acquisition costs, particularly as traditional tree-based models become increasingly complex with larger datasets, a CNN-based architecture is employed to reconstruct the complete admittance response from sparsely sampled data, including the real, imaginary, and magnitude components. As shown in

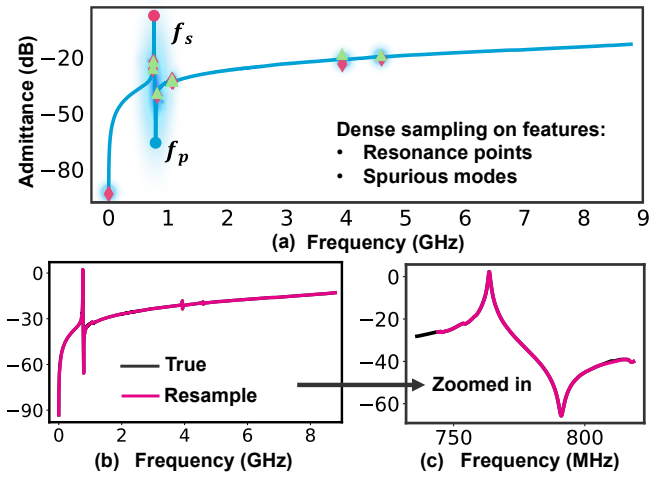


Fig. 15. Dense sampling at critical points improves spectrum fidelity: (a) feature-aware annotations for dense resampling; (b) accurate reconstruction of resonance features in the whole test frequency range; (c) zoomed-in near passband.

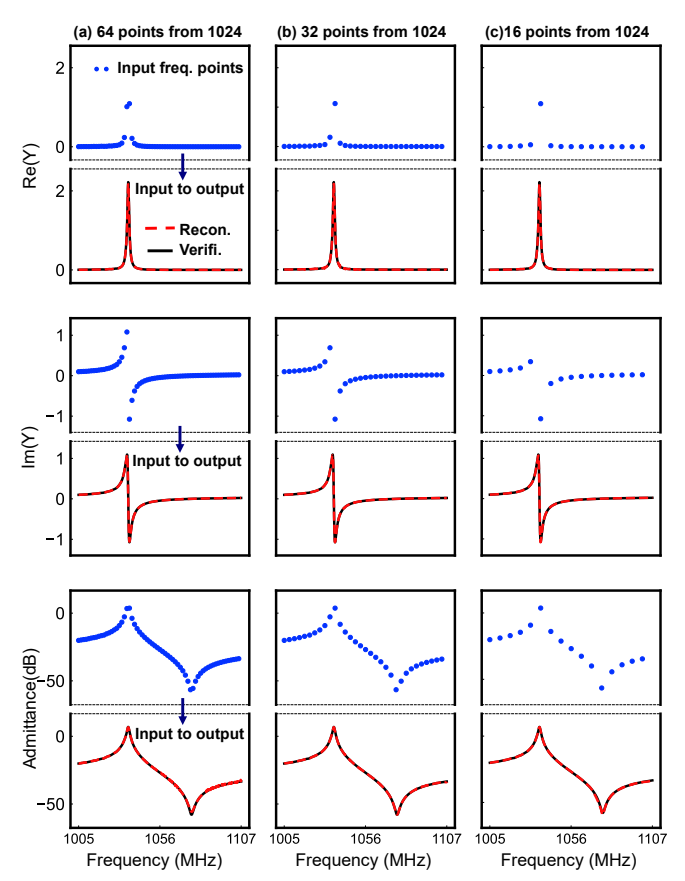


Fig. 16. Sparse-to-full reconstruction of complex admittance using 64, 32, and 16 points, which demonstrates strong reconstruction capability, even with highly compressed input.

Fig. 16, the model can recover the complete spectrum with high fidelity using only 16 uniformly spaced frequency points, representing a 98% reduction in resolution from the original 1,024-point input. The  $R^2$  score for all samples across the 25% test set remains above 0.98, validating the model's effectiveness in reducing both simulation and test-time bandwidth requirements without sacrificing spectral accuracy. This property makes the method particularly attractive in wafer-level testing scenarios, where reducing the number of VNA sweep points per device directly translates into shorter test times and lower cost.

## D. Sim-to-Real Framework for Small Size of Test Data

Collecting large volumes of measured data remains costly and time-consuming. In previous stages, our models were trained on a large industrial-scale dataset comprising 14,883 verified samples. In practice, however, such extensive measurement may not always be feasible. To reduce models' reliance on fabricated samples, a simulation-to-real (Sim-to-Real) learning algorithm is proposed. 10,000 simulated samples are first used as prior knowledge to capture the underlying structural–performance trends. Then, varying fractions of the 243-device measurement dataset are incorporated to compensate for the difference between simulation and tape-out. As shown in Fig. 17, the Sim-to-Real library consistently outperforms the traditional library trained solely on measured data (both *MSE* and *R*<sup>2</sup>), particularly

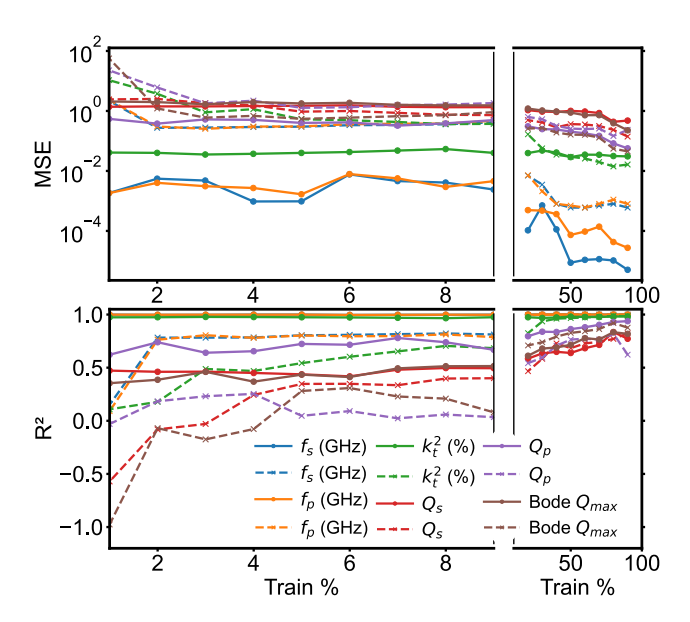


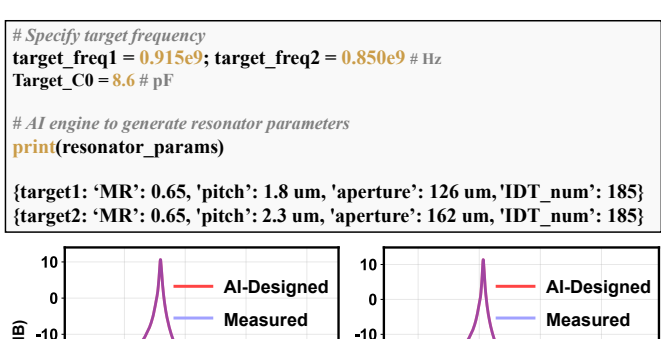
Fig. 17. Impact of training set size on MSE and R<sup>2</sup> score between a small amount of test data only (dotted line) and Sim-to-Real PDK (solid line).

when the available measurement data is limited. This is particularly relevant in early-stage prototyping or wafer-level yield estimation, where only a small subset of devices can be measured. This approach represents the first attempt to reduce the amount of measured data required for training task-specific models in MEMS acoustic resonators' design, thereby lowering experimental cost.

# E. Intelligent design example: Auto-Generation of the New Spurious-Free Design

Based on the preceding stages, an AI-assisted PDK is constructed by integrating simulation-driven predictions with measured device data. This library serves as a knowledge base that stores validated structure—performance mappings, enabling both forward prediction and inverse design. When a user specifies a target requirement, such as a desired resonance frequency range, high quality factor, or suppression of spurious responses, the system performs a direct query over the PDK and retrieves candidate resonator designs that satisfy these constraints.

As illustrated in Fig. 18, the design workflow allows interactive specification of performance targets followed by instant retrieval of matching device parameters. For example, when target series-resonance frequencies of 0.915 GHz  $(f_{measure} = 0.9148 \text{ GHz}) \text{ and } 0.850 \text{ GHz} (f_{measure} = 0.8516)$ GHz) with the same static capacitance ( $C_{0\_design} = 8.6 \text{ pF}$ ,  $C_{0 measure} = 8.601 \text{ pF}$ ) are specified, the AI engine synthesizes two previously unseen resonator designs, each characterized by a distinct set of structural parameters (metal ratio, pitch, aperture, and IDT number). Their predicted admittance spectra align closely with the measured curves from fabricated devices, indicating physical realizability and effective suppression of spurious responses. Crucially, these designs are generated rather than retrieved: they do not correspond to any existing entry in the PDK and thus expand the library with validated, spurious-free solutions tailored to



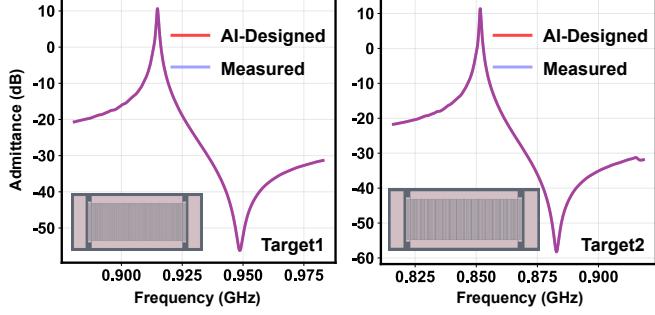


Fig. 18. Pseudocode workflow for AI-Assisted generation and validation results of new spurious-free resonators.

the requested targets.

## IV. CONCLUSION

This work presents an AI-driven design-test framework for MEMS acoustic resonators that systematically reduces reliance on multiphysics simulations and extensive wafer-level measurements. By incorporating regression-based parameter prediction, full-spectrum reconstruction, spurious mode quantification, and sparse recovery via CNNs, the framework achieves high predictive accuracy while substantially lowering computational and measurement costs. Experimental validation on a dataset of 14,883 industry-verified devices, 10,000 simulated structures, and 283 fabricated samples demonstrates that resonance and anti-resonance frequencies can be predicted with  $R^2 = 1.000$ , electromechanical coupling  $(k_t^2)$  and quality factors  $(Q_s, Q_p)$  with  $R^2 > 0.99$ , and full admittance spectra with mean squared error on the order of  $10^{-3}$ . The sparse spectrum recovery further reconstructs the complete admittance curve from as few as 16 frequency samples, corresponding to a 98% reduction in measurement density, while preserving  $R^2 > 0.98$ . A simulation-to-real transfer mechanism ensures robustness when limited experimental data are available, and all outputs are consolidated into an AI-assisted PDK that supports both forward prediction and reverse design: it can auto-generate previously unseen, spurious-free resonators that meet userspecified targets and match fabricated measurements, thereby converting the library from a passive repository into an active synthesis engine. These advances bridge simulation and fabrication, offering a scalable and validated solution for the intelligent design and testing of MEMS acoustic resonators.

#### ACKNOWLEDGMENT

The authors thank the National Natural Science Foundation of China (62304193), the Hong Kong Innovation and Technology Commission (ITS/144/23), and the Hong Kong

RGC Strategic Topic Grant (STG3/E-602/23N) for funding support. We acknowledge the help of the HKUST Nanosystem Fabrication Facility (CWB) in device fabrication.

#### REFERENCES

- [1] K. Yang, C. He, J. Fang, X. Cui, H. Sun, Y. Yang, and C. Zuo, "Advanced RF filters for wireless communications," *Chip*, vol. 2, no. 4, Art. no. 4, Dec. 2023, doi: 10.1016/j.chip.2023.100058.
- [2] J. Shen, S. Fu, R. Su, H. Xu, Z. Lu, Z. Xu, J. Luo, F. Zeng, C. Song, W. Wang, and F. Pan, "High-Performance Surface Acoustic Wave Devices Using LiNbO 3 /SiO 2 /SiC Multilayered Substrates," *IEEE Trans. Microwave Theory Techn.*, vol. 69, no. 8, Art. no. 8, Aug. 2021, doi: 10.1109/TMTT.2021.3077261.
- [3] S. Gong and G. Piazza, "Design and Analysis of Lithium—Niobate-Based High Electromechanical Coupling RF-MEMS Resonators for Wideband Filtering," *IEEE Trans. Microwave Theory Techn.*, vol. 61, no. 1, Art. no. 1, Jan. 2013, doi: 10.1109/TMTT.2012.2228671.
- [4] H. Nakamura, H. Nakanishi, R. Goto, and K. Hashimoto, "Suppression of transverse-mode spurious responses for saw resonators on SiO2/Al/LiNbO3 structure by selective removal of SiO2," *IEEE Transactions on Ultrasonics, Ferroelectrics, and Frequency Control*, vol. 58, no. 10, Art. no. 10, Oct. 2011, doi: 10.1109/TUFFC.2011.2068.
- [5] T. Omori, K. Matsuda, N. Yokoyama, K. Hashimoto, and M. Yamaguchi, "Suppression of transverse mode responses in ultra-wideband SAW resonators fabricated on a Cu-grating/15 degrees YX-linbO3 structure," *IEEE Trans Ultrason Ferroelectr Freq Control*, vol. 54, no. 10, pp. 1943–1948, Oct. 2007, doi: 10.1109/tuffc.2007.487.
- [6] T. Kimura, M. Kadota, and Y. Ida, "High Q SAW resonator using upperelectrodes on grooved-electrodes in LiTaO3," in 2010 IEEE MTT-S International Microwave Symposium, May 2010, pp. 1740–1743. doi: 10.1109/MWSYM.2010.5516895.
- [7] Q. Zhang, T. Han, W. Wang, K. Hashimoto, and J. Chen, "Surface acoustic wave propagation characteristics of ScAlN/diamond structure with buried electrode," in *Proceedings of the 2014 Symposium on Piezoelectricity, Acoustic Waves, and Device Applications*, Oct. 2014, pp. 271–274. doi: 10.1109/SPAWDA.2014.6998578.
- [8] R. Ro, R.-Y. Lee, H.-Y. Tung, and S. Wu, "Frequency Responses of SAW Ladder Filters with Apodized Interdigital Transducers and Width-Controlled Reflectors," in 2007 Sixteenth IEEE International Symposium on the Applications of Ferroelectrics, May 2007, pp. 742–745. doi: 10.1109/ISAF.2007.4393388.
- [9] G. Lv, Q. Zhang, S. Wu, T. Wu, B. Li, R. Lin, Z. Zhao, and F. Bao, "Study on Generation Mechanism of Harmonic Nonlinear Signals in LiNbO3/SiO2/Si SAW Resonators Based on Measurement and Simulation," *IEEE Transactions on Microwave Theory and Techniques*, pp. 1–10, 2025, doi: 10.1109/TMTT.2025.3579159.
- [10] Y. Liu, Y. He, Z. Yang, F. Li, J. Bao, and K.-Y. Hashimoto, "Study on Loss Mechanisms in SAW Resonators Using 42-LT Thin Plate by Full-3-D FEM With Hierarchical Cascading Technique," *IEEE Transactions on Ultrasonics, Ferroelectrics, and Frequency Control*, vol. 72, no. 4, pp. 539–546, Apr. 2025, doi: 10.1109/TUFFC.2025.3543541.
- [11] T. Takai, H. Iwamoto, Y. Takamine, H. Yamazaki, T. Fuyutsume, H. Kyoya, T. Nakao, H. Kando, M. Hiramoto, T. Toi, M. Koshino, and N. Nakajima, "High-Performance SAW Resonator on New Multilayered Substrate Using LiTaO3 Crystal," *IEEE Transactions on Ultrasonics, Ferroelectrics, and Frequency Control*, vol. 64, no. 9, pp. 1382–1389, Sep. 2017, doi: 10.1109/TUFFC.2017.2738119.
- [12] T. Takai, H. Iwamoto, Y. Takamine, T. Fuyutsume, T. Nakao, M. Hiramoto, T. Toi, and M. Koshino, "High-Performance SAW Resonator With Simplified LiTaO3/SiO2 Double Layer Structure on Si Substrate," *IEEE Transactions on Ultrasonics, Ferroelectrics, and Frequency Control*, vol. 66, no. 5, pp. 1006–1013, May 2019, doi: 10.1109/TUFFC.2019.2898046.
- [13] A. Kochhar, A. Mahmoud, Y. Shen, N. Turumella, and G. Piazza, "X-Cut Lithium Niobate-Based Shear Horizontal Resonators for Radio Frequency Applications," *J. Microelectromech. Syst.*, vol. 29, no. 6, Art. no. 6, Dec. 2020, doi: 10.1109/JMEMS.2020.3026167.
- [14] N. Matsuoka, T. Omori, and K. Hashimoto, "Suppression of Lowest-Order Plate Mode in Wafer-Bonded SAW Devices Using LiTaO<sub>3</sub> Thin

- Plate," in 2019 IEEE International Ultrasonics Symposium (IUS), Glasgow, United Kingdom, Oct. 2019, pp. 1231–1234. doi: 10.1109/ULTSYM.2019.8926253.
- [15] C. Thoma, "Fast COM parameter extraction from theoretically derived dispersion relations for SAWs propagating in periodic metallic gratings," in 1999 IEEE Ultrasonics Symposium. Proceedings. International Symposium (Cat. No.99CH37027), Oct. 1999, vol. 1, pp. 151–154 vol.1. doi: 10.1109/ULTSYM.1999.849374.
- [16] A. Shimko, H. Oh, and T. Sato, "Adaptation multimode COM for Low-Cut TC-SAW device," in 2024 IEEE Ultrasonics, Ferroelectrics, and Frequency Control Joint Symposium (UFFC-JS), Sep. 2024, pp. 1–4. doi: 10.1109/UFFC-JS60046.2024.10793712.
- [17] L. Zhang, S. Zhang, M. Sun, J. Wu, P. Zheng, X. Fang, D. Sui, and X. Ou, "Demonstration of Spurious-Free and Low-Loss X-Band SAW Filter," in 2024 IEEE Ultrasonics, Ferroelectrics, and Frequency Control Joint Symposium (UFFC-JS), Sep. 2024, pp. 1–4. doi: 10.1109/UFFC-JS60046.2024.10794040.
- [18] X. Liu, J. Zheng, Z. Ren, F. Qian, J. Xu, and Y. Yang, "Toward Interdigital Transducer-Based mmWave Acoustic: Mitigating Self-Resonances," in 2024 IEEE Ultrasonics, Ferroelectrics, and Frequency Control Joint Symposium (UFFC-JS), Sep. 2024, pp. 1–4. doi: 10.1109/UFFC-JS60046.2024.10794077.
- [19] X. Liu, J. Zheng, and Y. Yang, "Scale Interdigital Transducer-Based Microacoustic Resonators Into mmWave Applications," *IEEE Transactions on Ultrasonics, Ferroelectrics, and Frequency Control*, vol. 72, no. 5, pp. 674–685, May 2025, doi: 10.1109/TUFFC.2025.3554004.
- [20] Y. Yan, K. Huang, H. Zhou, X. Zhao, W. Li, Z. Li, A. Yi, H. Huang, J. Lin, S. Zhang, M. Zhou, J. Xie, X. Zeng, R. Liu, W. Yu, T. You, and X. Ou, "Wafer-Scale Fabrication of 42° Rotated Y-Cut LiTaO3-on-Insulator (LTOI) Substrate for a SAW Resonator," ACS Appl. Electron. Mater., vol. 1, no. 8, pp. 1660–1666, Aug. 2019, doi: 10.1021/acsaelm.9b00351.
- [21] W. Liu, Q.-J. Zhang, F. Feng, X. Wang, J. Xue, J. Zhang, and K. Ma, "Electromagnetic Parametric Modeling Using MOR-Based Neuro-Impedance Matrix Transfer Functions for Two-Port Microwave Components," *IEEE Transactions on Microwave Theory and Techniques*, vol. 72, no. 5, pp. 2973–2989, May 2024, doi: 10.1109/TMTT.2023.3330766.
- [22] O. Akinwande, X. Jia, A. Deroo, Y. Lu, H. Lin, B.-C. Tseng, and M. Swaminathan, "Transfer Learning Framework for 3-D Electromagnetic Applications," *IEEE Transactions on Microwave Theory and Techniques*, vol. 73, no. 8, pp. 4490–4500, Aug. 2025, doi: 10.1109/TMTT.2025.3525986.
- [23] F. Sui, W. Yue, R. Guo, K. Behrouzi, and L. Lin, "Designing Weakly Coupled Mems Resonators with Machine Learning-Based Method," in 2022 IEEE 35th International Conference on Micro Electro Mechanical Systems Conference (MEMS), Jan. 2022, pp. 454–457. doi: 10.1109/MEMS51670.2022.9699450.
- [24] L. Zhang, Q. Wang, S. Zhao, D. Liu, C. Li, B. Wang, and X. Wang, "Deep-Learning-Based Microwave-Induced Thermoacoustic Tomography Applying Realistic Properties of Ultrasound Transducer," *IEEE Transactions on Microwave Theory and Techniques*, vol. 72, no. 10, pp. 5983–5993, Oct. 2024, doi: 10.1109/TMTT.2024.3439551.
- [25] B. Zuo, Z. Wu, J. Zhao, B. Niu, Y. Lei, L. Cao, Y. Zhu, and J. Yang, "Bi-Mode Inverse Design of 3D Structures for MEMS Resonators," *IEEE Electron Device Letters*, vol. 46, no. 5, pp. 841–844, May 2025, doi: 10.1109/LED.2025.3548612.
- [26] X. Ke, J. Wu, S. Zhang, X. Fang, P. Zheng, L. Zhang, D. Ling, J. He, K. Huang, and X. Ou, "Predefined Novel Piezo-On-Insulator (PN-POI) Substrates for 5G/6G Acoustic Devices," in 2024 IEEE International Electron Devices Meeting (IEDM), San Francisco, CA, USA, Dec. 2024, pp. 1–4. doi: 10.1109/IEDM50854.2024.10873455.
- [27] W. Fang, J. Wang, Y. Lu, S. Liu, Y. Wu, Y. Ma, and Z. Xie, "A Survey of Circuit Foundation Model: Foundation AI Models for VLSI Circuit Design and EDA." arXiv, Mar. 28, 2025. doi: 10.48550/arXiv.2504.03711.
- [28] C. Wang, F. Yang, and K. Zhu, "AI-Enabled Layout Automation for Analog and RF IC: Current Status and Future Directions," in 2024 IEEE International Symposium on Radio-Frequency Integration Technology (RFIT), Chengdu, China, Aug. 2024, pp. 1–3. doi: 10.1109/RFIT60557.2024.10812465.
- [29] A. J. Gabourie, C. A. Polanco, C. J. McClellan, H. Su, M. Malakoutian, Ç. Köroğlu, S. Chowdhury, D. Donadio, and E. Pop, "AI-Accelerated Atoms-to-Circuits Thermal Simulation Pipeline for Integrated Circuit

- Design," in 2024 IEEE International Electron Devices Meeting (IEDM), San Francisco, CA, USA, Dec. 2024, pp. 1–4. doi: 10.1109/IEDM50854.2024.10873564.
- [30] K. Yang, J. Chen, and C. Zuo, "11.6-GHz SV-SAW Resonator Based on Y128° LiNbO3/SiO2/Si Substrate," in 2024 IEEE Ultrasonics, Ferroelectrics, and Frequency Control Joint Symposium (UFFC-JS), Sep. 2024, pp. 1–4. doi: 10.1109/UFFC-JS60046.2024.10793705.
- [31] J. Karim, A. N. Nordin, A. Z. Alam, and U. Hashim, "Pierce oscillator circuit topology for high motional resistance CMOS MEMS SAW resonator," in 2012 10th IEEE International Conference on Semiconductor Electronics (ICSE), Sep. 2012, pp. 254–258. doi: 10.1109/SMElec.2012.6417135.
- [32] "Design of A SAW Duplexer Based on Al/LN/SiO2/4H-SiC Multi-layer Film Structure | IEEE Conference Publication | IEEE Xplore." https://ieeexplore.ieee.org/document/10470055 (accessed Aug. 27, 2025).
- [33] D. R. Gallagher, M. W. Gallagher, N. Saldanha, J. M. Pavlina, and D. C. Malocha, "Spread Spectrum Orthogonal Frequency Coded SAW Tags and Sensors Using Harmonic Operation," *IEEE Transactions on Microwave Theory and Techniques*, vol. 58, no. 3, pp. 674–679, Mar. 2010, doi: 10.1109/TMTT.2010.2040347.
- [34] D. Royer and T. Valier-Brasier, Elastic Waves in Solids 1: Propagation, 1st ed. Wiley, 2022. doi: 10.1002/9781119902942.
- [35] K. Hashimoto, Ed., RF bulk acoustic wave filters for communications. Boston London: Artech House, 2009.
- [36] S. R. Arumugam, S. Gowr, Abimala, Balakrishna, and O. Manoj, "Performance Evaluation of Machine Learning and Deep Learning Techniques," in *Convergence of Deep Learning in Cyber-IoT Systems and Security*, Wiley, 2023, pp. 21–65. doi: 10.1002/9781119857686.ch2.
- [37] A. Krizhevsky, I. Sutskever, and G. E. Hinton, "ImageNet Classification with Deep Convolutional Neural Networks," in Advances in Neural Information Processing Systems, 2012, vol. 25. Accessed: Aug. 28, 2025. [Online]. Available: https://proceedings.neurips.cc/paper/2012/hash/c399862d3b9d6b76c8436 e924a68c45b-Abstract.html
- [38] K. Simonyan and A. Zisserman, "Very Deep Convolutional Networks for Large-Scale Image Recognition." arXiv, Apr. 10, 2015. doi: 10.48550/arXiv.1409.1556.
- [39] K. He, X. Zhang, S. Ren, and J. Sun, "Deep Residual Learning for Image Recognition," presented at the Proceedings of the IEEE Conference on Computer Vision and Pattern Recognition, 2016, pp. 770–778. Accessed: Aug. 28, 2025. [Online]. Available: https://openaccess.thecvf.com/content\_cvpr\_2016/html/He\_Deep\_Residu al\_Learning\_CVPR\_2016\_paper.html
- [40] M. Lu, X. Xiao, Y. Pang, G. Liu, and H. Lu, "Detection and Localization of Breast Cancer Using UWB Microwave Technology and CNN-LSTM Framework," *IEEE Transactions on Microwave Theory and Techniques*, vol. 70, no. 11, pp. 5085–5094, Nov. 2022, doi: 10.1109/TMTT.2022.3209679.
- [41] O. Ronneberger, P. Fischer, and T. Brox, "U-Net: Convolutional Networks for Biomedical Image Segmentation." arXiv, May 18, 2015. doi: 10.48550/arXiv.1505.04597.
- [42] J. Zheng, J. Xu, F. Qian, and Y. Yang, "Over-1 GHz Bandwidth Filter Based on Y-128° Cut Lithium Niobate on Amorphous Silicon," in 2024 IEEE 37th International Conference on Micro Electro Mechanical Systems (MEMS), Austin, TX, USA, Jan. 2024, pp. 36–39. doi: 10.1109/MEMS58180.2024.10439472.